

A COMPLETE CENSUS OF $H\alpha$ EMITTERS IN NGC 6397CRISTINA PALLANCA^{1,2}, GIACOMO BECCARI³, FRANCESCO R. FERRARO^{1,2}, LUCA PASQUINI³, BARBARA LANZONI^{1,2}, ALESSIO MUCCIARELLI^{1,2}*Draft version January 20, 2022*

ABSTRACT

We used a dataset of archival Hubble Space Telescope images obtained through the F555W, F814W and F656N filters, to perform a complete search for objects showing $H\alpha$ emission in the globular cluster NGC 6397. As photometric diagnostic, we used the $(V-H\alpha)_0$ color excess in the $(V-H\alpha)_0$ – $(V-I)_0$ color-color diagram. In the analysed field of view, we identified 53 $H\alpha$ emitters. In particular, we confirmed the optical counterpart to 20 X-ray sources (7 cataclysmic variables, 2 millisecond pulsars and 11 active binaries) and identified 33 previously unknown sources, thus significantly enlarging the population of known active binaries in this cluster. We report the main characteristics for each class of objects. Photometric estimates of the equivalent width of the $H\alpha$ emission line, were derived from the $(V-H\alpha)_0$ -excess and, for the first time, compared to the spectroscopic measurements obtained from the analysis of MUSE spectra. The very good agreement between the spectroscopic and photometric measures fully confirmed the reliability of the proposed approach to measure the $H\alpha$ emission. The search demonstrated the efficiency of this novel approach to pinpoint and measure $H\alpha$ -emitters, thus offering a powerful tool to conduct complete census of objects whose formation and evolution can be strongly affected by dynamical interactions in star clusters.

Subject headings: globular clusters: general — globular clusters: individual (NGC 6397)

1. INTRODUCTION

The crowded cores of globular clusters (GCs) are very efficient “furnaces” for generating exotic objects, such as cataclysmic variables (CVs), low-mass X-ray binaries (LMXBs), millisecond pulsars (MSPs) and blue stragglers (see Bailyn 1995). Most of these objects are thought to be the result of the evolution of various kinds of binary systems originated and/or hardened by stellar interactions (Davies 2005; Ivanova et al. 2006). The nature and even the existence of binary by-products are strongly related to the cluster core dynamics (Ferraro et al. 2003, 2009, 2015a). Hence a complete census of these objects (whose formation and evolution are strongly affected by dynamical interactions) is crucial in order to trace the dynamical evolution of the parent cluster (Beccari et al. 2006; Ferraro et al. 2012; Lanzoni et al. 2016).

Most of these exotic objects are expected to be, at least, potential $H\alpha$ emitters. LMXBs are binary systems made of a compact object (a stellar black hole or a neutron star; NS) accreting mass from a low mass companion through an accretion disk. They are usually bright X-ray sources and, in the case of a NS compact object, they are thought to be the progenitors of MSPs. MSPs form in binary systems containing a NS first evolved through the LMXB phase and then eventually spun up to millisecond periods by mass accretion from the evolving companion (see e.g. Ferraro et al. 2015b), that, in turn, is expected to become a white dwarf (e.g. Lyne et al. 1987; Alpar et al. 1982; Bhattacharya & van den Heuvel 1991). However, in the last years the number of detections of non-degenerate companions significantly increased (Pallanca et al. 2010, 2013, 2014; Cadelano et al. 2015). Note that the first non-degenerate com-

panion to a MSP in a GC (PSR J1740–5340A) was found by Ferraro et al. (2001) in NGC 6397 (the cluster subject of this paper).

MSPs usually do not have strong $H\alpha$ excess, since accretion is inhibited by the presence of a strong magnetic field. However, in the cases of transitional-MSPs (T-MSPs), which are thought to be the evolutionary link between LMXBs and MSPs, a significant $H\alpha$ emission is not unexpected and it has been indeed confirmed in the case of PSR J1824–2452I in the GC M28 (Pallanca et al. 2013) as well as in the Redback system PSR J1740–5340A in NGC6397 (Ferraro et al. 2001; Sabbi et al. 2003).

CVs are binary systems in which a white dwarf is accreting material from a main sequence (MS) companion (see Knigge 2012, for a review). From the theoretical point of view, models predict that there should be 60–180 CVs for every $10^6 L_{\odot}$ in an old stellar population (Townsend & Bildsten 2005), most of which should be formed dynamically (Ivanova et al. 2006). Several methods have been proposed to detect candidate CVs (Knigge 2012): (i) studying the variability associated to dwarf nova outbursts; (ii) looking for objects showing bluer colors than MS stars, because of the energy released in a hot region close to the white dwarf; (iii) searching for the X-ray emission produced by the accretion onto the compact object; (iv) spectroscopically detecting emission lines. However, none of these methods is able to recover the entire CV population expected and in most cases more than one method is needed to properly classify the objects. Beccari et al. (2014) showed that the detection of candidate CVs as sources showing $H\alpha$ excess emission in GCs can be improved by using a proper combination of broad bands V and I and narrow band $H\alpha$ imaging. This method was successfully applied in star-forming regions (see De Marchi et al. 2010) and in other clusters (see Pallanca et al. 2013) to identify $H\alpha$ emitters.

It is worth mentioning that, in addition to the classes of interacting binaries described above, in which the $H\alpha$ excess is related to the mass transfer process, there are other objects

¹ Dipartimento di Fisica e Astronomia, Alma Mater Studiorum Università di Bologna, Via Gobetti 93/2, I-40129 Bologna, Italy

² INAF-Osservatorio Astronomico di Bologna, Via Gobetti 93/3, I-40129 Bologna, Italy

³ European Southern Observatory, Karl-Schwarzschild-Strasse 2, 85748 Garching bei München, Germany

which are expected to show $H\alpha$ emission, because of their intense chromospheric activity: the so-called active binaries (ABs). The two most relevant prototypes of this category of objects are RS Canum Venaticorum and BY Draconis (BY Dra) binaries. Indeed a large population of BY Dra-type binaries has been found in NGC6397 (see Taylor et al. 2001; Cohn et al. 2010).

In this paper we applied the $(V-H\alpha)_0 - (V-I)_0$ color-color method to identify $H\alpha$ emitters and to derive a photometric estimate of the $H\alpha$ Equivalent Width (EW).

2. THE TARGET CLUSTER: NGC6397

In the framework of the study of exotic populations in dense stellar systems, NGC 6397 is an ideal GC to be studied, because its X-ray population is already known and classified. Thanks to deep Chandra imaging of the cluster, Grindlay et al. (2001) detected 25 X-ray sources with $L_x > 3 \times 10^{29}$ erg s^{-1} located within $2'$ from the cluster center. In a more recent work Bogdanov et al. (2010) identified 79 Chandra X-ray sources that lie within the half-mass radius ($r_h = 2'.33$ Harris 1996), of which, 15 are CVs, 42 are ABs, 1 is a radio detected MSP and 1 is a candidate MSP (Cohn et al. 2010). The comparison between the MSP and CV populations of NGC 6397 and 47 Tuc shows that the CV to MSP ratio is ~ 10 times larger in NGC 6397, thus suggesting a dichotomy of compact objects and binary production in the two clusters: NGC 6397 has overproduced CVs (for its mass), perhaps because of two-body captures during core collapse, while its relatively lower MSP production might be due to a lower NS retention or original fraction due to differences in the cluster initial mass functions, in turn due to their very different metallicities (Grindlay et al. 2001).

The CV population of NGC 6397 has been identified with different methods: CVs 1-3 were originally identified in a HST $H\alpha$ survey (Cool et al. 1995), CVs 4-5 were found via optical variability or as counterparts to ROSAT HRI sources (Cool et al. 1998; Grindlay 1999), CVs 6-8 were discovered in a deeper follow-up HST $H\alpha$ survey (Grindlay et al. 2001), CV9 has been identified on the basis of its Chandra spectrum, and the remaining CVs have been detected as Chandra X-sources (Bogdanov et al. 2010).

A spectroscopic confirmation through hydrogen and helium lines has been obtained for four objects (CVs 1-4; Grindlay et al. 1995; Edmonds et al. 1999). All these CVs show $HeII\lambda 4686$, a line seen almost exclusively in magnetic CVs and nova-like variables. For CV2 and CV3 the authors also observed nova-like eruptions, which are unexpected for magnetic CVs, since the magnetic field should prevent the disk instability that leads to the nova phenomenon.

Variability has been detected in CVs 1–9, and in two cases it has been found to be particularly strong: CV2 shows a variability of at least 2.7 mag and CV3 is seen 1.8 mag brighter in eruption than in quiescence (Shara et al. 2005). On the other hand CV1 and CV6 were identified as eclipsing CVs by Kaluzny et al. (2003). The light curves of both of them exhibit two distinct minima per orbital period and they seem to be dominated by ellipsoidal variations. The accretion rate in CV6 has been roughly constant over the observing seasons 2002–2004 (Kaluzny et al. 2006).

Cohn et al. (2010) showed the location of the CV candidates in the color-magnitude diagrams (CMDs) and suggested that there is an evolutionary sequence from young, bright CVs, to old, faint ones. The optical emission of the six brightest CVs appears to be dominated by a relatively massive sec-

ondary, while that of the faint CVs is mainly due to the white dwarfs, with very little contribution from a very low-mass secondary. CVs 1–6 are the young, recently formed systems.

Cohn et al. (2010) reported on the detection of 42 candidate ABs, of which 25 lie within the field covered with the data used in this work. Most of them draw a relatively homogenous binary sequence alongside the MS (Cohn et al. 2010) and according to Taylor et al. (2001) they are likely BY Dra objects.

In this paper we applied the selection method of $H\alpha$ emitters commonly used in star forming regions (De Marchi et al. 2010) and recently applied to GCs (Beccari et al. 2014; Pallanca et al. 2013) as a tool to both identify exotic objects and derive a photometric estimate of the EW (pEW) of the $H\alpha$ emission.

3. OBSERVATIONS AND DATA REDUCTION

The data used in this work (GO 7335 PI Grindlay) consist of 88 images obtained with the Wide Field Planetary Camera 2 (WFPC2) in the broad F555W and F814W bands and the narrow F656N filter (hereafter V , I and $H\alpha$ respectively).

We analysed the entire set of images through a standard point spread function (PSF) fitting procedure by using DAOPHOT/ALLFRAME (Stetson 1987). In short, we calculated a PSF model on each image using approximately 50 isolated and not saturated stars. We then used the DAOPHOT/MONTAGE2 routine to stack all the V and I images together. In this way we obtained 4 very deep and very high signal-to-noise ratio images (one for each CCD of the WFPC2 detector) cleaned of cosmic rays and detector blemishes. We extracted a list of stellar sources from these reference images and we used it as input master list of ALLFRAME (Stetson 1994), which simultaneously determines the star brightness in all frames. As last step, the magnitude of each star in each band was obtained as the average of at least 4 measures, while the standard deviation of the repeated measures was taken as photometric error. We calibrated the WFPC2 magnitudes into the VEGAMAG system using the standard recipe and zeropoints reported in Holtzman et al. (1995). Finally, we de-reddened all observed magnitudes by assuming a color excess $E(B-V) = 0.18$ (Gratton et al. 2003; Richer et al. 2008).

We show in Figure 1 the reddening-corrected V_0 vs. $(V-I)_0$ CMD obtained from the WFPC2 photometric catalog (gray points). The cluster's stars are sampled from the bottom of the red giant branch down to ~ 7 magnitudes below the MS Turn off ($V_0 \sim 16.2$). The best-fit isochrone (Dotter et al. 2008), obtained for an age=13.5 Gyr, a metallicity $[Fe/H]=-2.03$ and $[\alpha/Fe]=0.4$ (Richer et al. 2008), and assuming a distance modulus $(m-M)_0 = 12.01$ (Gratton et al. 2003) is also shown in Figure 1 (solid line). The isochrone has been used to convert the sampled magnitudes into stellar masses. As shown in Figure 1 we are able to sample the MS stars from $0.75 M_\odot$ (corresponding to the mass of stars at the Turn off) down to $0.2 M_\odot$ at the bottom of the MS.

We finally transformed the relative stellar positions into absolute Right Ascension (RA) and Declination (Dec) using more than 300 stars in common with a photometric catalog (Ferraro et al. 2001) from ground-based images obtained with the Wide Field Imager (WFI) at the 2.2m telescope at La Silla. This allowed us to obtain a global astrometric accuracy of $0''.3$ in both RA and Dec. It is worth to notice that the same astrometric accuracy allowed Ferraro et al. (2001) to identify the optical counterpart of the MSP J1740–5340 in the same HST WFPC2 dataset used in this paper.

4. SELECTION OF H α EMITTERS AND EQUIVALENT WIDTH MEASURE

4.1. Photometric approach

We used the method described in De Marchi et al. (2010) and recently applied to GCs by Beccari et al. (2014) and Pallanca et al. (2013) in order to identify all objects showing H α excess in the WFPC2 field of view. In Figure 2 we show as gray points the position of all the stars with magnitude fainter than the MS Turn off in the $(V-H\alpha)_0$ vs $(V-I)_0$ color-color diagram. Note that with this color combination we can both reproduce the continuum for different spectral types and provide a good estimate of the H α emission, being the H α line contribution to the V band negligible. As expected, the vast majority of MS stars shows very low (if any) H α excess emission. As a consequence in the $(V-H\alpha)_0$ vs $(V-I)_0$ plane they define a very narrow sequence, which empirically indicates the locus of stars with no H α emission. The conversion of the $(V-I)_0$ colors into stellar temperatures and spectral types indicated in the figure is done using the atmospheric model of Bessell et al. (1998, gray triangles). To first select objects with H α excess and then estimate the pEW of the emission we calculated a reference line, for the stars not showing H α excess, defined as the median $(V-H\alpha)_0$ color of stars with a combined photometric error (computed as $\sigma_{(V-H\alpha)_0} = \sqrt{\sigma_V^2 + \sigma_{H\alpha}^2}$) smaller than 0.05 mags. It is important to note that the empirical relation (gray solid line in the Figure 2) agrees very well with the theoretical one from the atmospheric model of Bessell et al. (1998). For each source, we measured the "color" difference ($\Delta(V-H\alpha)_0$) between the observed $(V-H\alpha)_0$ color and the value of $(V-H\alpha)_0$ measured along the reference line at the source $(V-I)_0$. We then selected as candidate H α emitters those objects with $\Delta(V-H\alpha)_0$ at least five times larger than the source intrinsic error (see Figures 3). The use of such a conservative threshold guarantees to avoid the selection of objects showing a "fake" color excess, that is actually due to a large intrinsic photometric error. We performed a visual inspection of each candidate H α emitter onto the stacked images in order to exclude objects possibly contaminated from close saturated stars. This procedure allowed us to reject almost half of the initially selected candidates.

We accepted as bona fide H α emitters also the objects with $(V-H\alpha)_0$ color excess 4 times larger than the intrinsic error, but falling within 0".5 from the nominal position of a X-ray source. In this way we added 4 more objects to the previous selection (See stars marked by asterisks in Figure 3 and 4). Following this approach we identified 53 candidate H α emitters: their coordinates and magnitudes are listed in Table 1, and their position in the $(V, V-I)$ -CMD is shown in Figure 5.

We then reported the position of these objects in the color-color diagram (Figure 4), the ideal plane to directly measure the pEW of the emission. For all the selected bona-fide H α emitters, we derived a pEW estimation of the H α emission line following equation (4) in De Marchi et al. (2010): $\text{pEW} = \text{RW} \times [1 - 10^{(-0.4 \times \Delta H\alpha)}]$, where RW is the rectangular width of the filter in Å units, which depends on the specific characteristics of the filter (see Table 4 in De Marchi et al. 2010). The obtained values are listed in Table 1 and reported in Figure 6 as a function of the $(V-I)_0$ color. The 8 faintest (with $V_0 > 22$) objects without a X-ray counterpart, for which the photometric errors are larger than $\sigma_{(V-H\alpha)_0} > 0.05$ mag are considered "low confidence candidates" and for this rea-

son they are plotted as open circles in Figures 3, 4, 5 and 6.

4.2. Comparison with MUSE

Very recently Husser et al. (2016) presented the spectroscopic analysis of more than 12,000 stars in NGC 6397 observed with the VLT-MUSE, a panoramic integral-field spectrograph able to acquire low resolution spectra ($R = 2000 - 4000$, from the bluest to the reddest wavelengths) in the range $0.465 - 0.93 \mu\text{m}$ (Bacon et al. 2014). While most of the H α emitters selected through our photometric strategy fall below the MUSE detection threshold, we were able to retrieve the spectra of 20 sources in common with our photometric catalog. They have been used to obtain a spectroscopic estimate of the H α EW (sEW), for a direct comparison with our photometric values (pEWs).

From the best-fit isochrone, we assigned a temperature and a surface gravity to each target. These have then been used to calculate a synthetic spectrum with the SYNTH code developed by R. L. Kurucz. After the convolution with a Gaussian profile, needed to reproduce the spectral resolution of MUSE, we determined the radial velocity of each target through cross correlation (by using the iraf task fxcor) with the synthetic spectrum in the Calcium triplet region, and we reported the observed spectra to the rest frame. In the following comparison with MS stars, the shift to the rest frame is fundamental because, being members of binary systems, the H α emitters can have a radial velocity significantly different from GC systemic velocity and variable along orbital phase. We then adopted the same approach to analyse a sample of MS stars with comparable temperature and gravity, and once reported to the zero velocity rest frame, we built a reference median template through the IRAF task scombine. Finally, because for most objects the H α line in the atmosphere of the H α emitters just appears as a less absorbed feature with respect to what observed in unperturbed stars with similar physical parameters, we divided the target spectra by the reference template, in order to isolate the emission component, and we measured the sEW through a Gaussian fit. In some cases the line profile was asymmetric (likely due to H α emission coming from different regions of the system; e.g. see Sabbi et al. 2003) and a minor, secondary Gaussian component was used in the fit.

In order to estimate the uncertainties in the sEW measures we performed Monte Carlo simulations. We first simulated 5 templates with different H α sEWs (1, 3, 5, 10 and 50 Å). For each template we built a set of simulated spectra with variable signal to noise ratio (SNR), ranging from 5 to 50 in steps of 5. Then we ran an automatic procedure able to measure the sEW in each set of simulated spectra. Thus the dispersion of the sEW measures was derived as a function of both the measured sEW and the spectrum SNR. This grid of values was used to derive the uncertainty of each H α sEW measured in a spectrum of a given SNR. The values obtained are reported in Table 1.

For CV1 and eight ABs, two different MUSE spectra are available in the Husser et al. (2016) data-set and we thus obtained two measures. For the eight ABs the two values agree each other within $1 - \sigma$ uncertainties. In the case of (the main component of) CV1, we obtain 14 and 27.1 Å, while Edmonds et al. (1999) found 21 Å from HST spectroscopy. These differences are likely due to intrinsic variability of the emission and the time difference between the observations. All the sEWs thus obtained are listed in Table 1, where we

also report the values quoted in Table 1 of Edmonds et al. (1999) for CVs 1–4.

As shown in Figure 7, we find a general good agreement between the photometric and the spectroscopic measurements of the $H\alpha$ EW for the stars in common with the MUSE catalog. The largest discrepancies are found for CVs (note that the axes in the figure are logarithmic), and can again be explained by the intrinsic variability of their $H\alpha$ emission and by taking into account that the WFPC2 and the MUSE observations of the cluster have been performed in very different epochs (the photometric and the spectroscopic data were acquired in April 1999 and July 2014, respectively). This comparison is critical since it provides the first direct test of the fact that a combination of broad band with narrow band $H\alpha$ imaging allows to obtain reliable photometric measurements of EW of stars showing $H\alpha$ excess. This is particularly critical in regions where severe stellar crowding or target faintness prevents to obtain reliable spectroscopic data.

5. DISCUSSION

Using the selection criteria described in the previous section we found 53 objects with $H\alpha$ excess. Through cross-correlation with catalogs of peculiar sources in this GC (i.e. X-ray sources, and variable stars; Cohn et al. 2010 and Kaluzny et al. 2003, respectively) we were able to find associations with previously known objects. In particular we found that 20 $H\alpha$ emitters (7 CVs, 2 MSPs and 11 ABs) have an X-ray counterpart. Moreover, 8 objects (among the brightest) were identified as variable stars and 9 sources were previously classified as BY Dra-type binaries. The remaining 33 candidates are new sources. We stress here that the eight faintest objects (without a X-ray counterpart) are however considered uncertain because of the large photometric errors. See Table 1 for a summary.

All the 7 detected CVs show a pEW larger than 15 Å. In particular they appear to be divided in two groups: CV4 and CV5 have pEW larger than 80 Å, while CV1, CV2, CV3, CV6 and CV7 show an average $H\alpha$ excess (pEW \sim 25 Å). Such a dichotomy is suggestive of a different evolutionary state (Pallanca et al. 2013) or a different accretion state (likely depending on the nature of the compact object). In fact, even if they are classified as CVs, we cannot definitely rule out the hypothesis that some of them could be T-MSPs, similar to PSR J1023+0038 and PSR J1227–4853 (Stappers et al. 2014; Roy et al. 2015). In the CMD (see Figure 5) they are located both on the left and on the right side of the MS. This evidence confirms that the CMD position alone (e.g. a color bluer than the MS) cannot be exhaustively used to select a complete sample of CVs and that the pEW that we can measure with the observational method described in this paper is indeed critical.

Interestingly all the 11 ABs found in our catalog show a pEW smaller than 4 Å and lie on the sequence of binary systems observed on the red side of the MS (see Figure 5). Note also that while they all have X-ray counterparts known, only 7 were previously identified in optical bands as possible BY Dra binaries (Taylor et al. 2001; see also Table 1), thus suggesting that the $H\alpha$ selection method allowed us to detect 4 more ABs (\sim 50% more) with respect to the optical variability study.

We performed a Kolmogorov-Smirnov test comparing the radial distributions of X-ray CVs, X-ray ABs and MS stars. We found that both the CVs and the ABs are more concentrated than MS stars (see Figure 8). In particular the probability that they are extracted from the same parent popu-

lation of MSs is only of the order of 0.1–0.2%, while the radial distributions of ABs is compatible with that of CVs with a probability of 28%. Finally, the two MSPs (the radio known U12 and the candidate U18) have a small pEW, slightly larger than the values measured for the ABs. This is a further confirmation that source U18 is very similar to U12 (PSR J1740–5340A) and it well fits within the scenario already proposed by Bogdanov et al. (2010) who found that its X-ray and optical properties are consistent with those of a binary containing a rotation-powered pulsar wind interacting with material from the secondary star.

Among the sources without a X-ray counterpart, only one object is known in the literature and it is classified as a possible BY Dra-type binary (star number 10 in Table 1). Eleven of the $H\alpha$ emitters with no X-ray counterpart have a pEW $<$ 4 Å and a CMD position compatible with the sequence of binaries. This suggests that they are likely ABs. The remaining objects, showing pEW larger than 4 Å could be unknown interacting binaries (MSPs or CVs). Their classification remains uncertain at the moment, however they surely are primary targets for further investigation.

6. SUMMARY AND FUTURE PERSPECTIVES

By using a set of high-resolution images of the central region of the GC NGC 6397, acquired through the V , I , $H\alpha$ filters we identified 53 objects with $H\alpha$ excess. Among them there are 20 X-ray sources: 7 CVs, 11 ABs, 1 radio MSP and 1 candidate MSP. In particular all the ABs have a pEW smaller than 4 Å and in the CMD they are located onto the cluster binary sequence. The two MSPs are both located below the Sub Giant Branch and have a pEW of emission slightly larger than that of ABs. The CVs are mostly out of canonical sequences in the CMD, both on the left and on the right side of the MS, and they have a significantly large $H\alpha$ emission (pEW $>$ 15 Å) suggesting that for these objects the source of emission is an accretion process, instead of chromospheric activity (as likely is in ABs). The CVs seem to have two different regimes of accretion. In particular CV4 and CV5 are characterised by a strong $H\alpha$ similarly to the peculiar T-MSP J1824–2452I in M28 (Pallanca et al. 2013). We also detected several objects with no X-ray counterparts: these objects can be ABs and or interacting binaries.

In this paper we used an innovative method to estimate the EW through photometric observations. The derived values have been found to nicely correlate with the spectroscopic measurements, thus confirming the reliability of the photometric approach. Such a method allows to detect new objects with $H\alpha$ excess and, in principle, to measure the emission EW also from objects which are too faint to be target of spectroscopic observations.

Note that the proposed selection method could play a fundamental role in the detection of T-MSPs. For example the two known field T-MSPs were initially misidentified as magnetic CVs (Bond et al. 2002; Butters et al. 2008). In particular T-MSPs during their life likely changes significantly the amount of $H\alpha$ excess (i.e. during quiescent state PSR J1824–2452I shows a pEW of a few Å, as the ABs, while during burst phase it is characterised by strong emission, even larger than some CVs).

An important step forward will be to obtain similar dataset in different epochs in order to identify objects (as T-MSPs, active LMXB and CVs) that are significantly changing status along time. Moreover also coordinated photometric and spec-

troscopic observations planned at the same time would be important in order to further test the correlation between pEW and sEW without the bias of intrinsic variability of accretion.

ACKNOWLEDGMENTS

We thank the anonymous referee for the careful reading of the manuscript and useful comments. C.P. warmly thanks the

support of the ESO Visitor Program. The research leading to these results has received funding from the European Community's Seventh Framework Programme (FP7/2007-2013/) under grant agreement No 229517. Based on observations made with the NASA/ESA Hubble Space Telescope, obtained from the data archive at the Space Telescope Institute. STScI is operated by the association of Universities for Research in Astronomy, Inc. under the NASA contract NAS 5-26555.

Facilities: ESO (WFI), HST (WFPC2).

REFERENCES

- Alpar, M. A., Cheng, A. F., Ruderman, M. A., & Shaham, J. 1982, *Nature*, 300, 728
- Bailyn, C. D. 1995, *ARA&A*, 33, 133
- Bhattacharya, D., & van den Heuvel, E. P. J. 1991, *Phys. Rep.*, 203, 1
- Bacon, R., Vernet, J., Borisova, E., et al. 2014, *The Messenger*, 157, 13
- Beccari, G., Ferraro, F. R., Possenti, A., et al. 2006, *AJ*, 131, 2551
- Beccari, G., De Marchi, G., Panagia, N., & Pasquini, L. 2014, *MNRAS*, 437, 2621
- Bessell, M. S., Castelli, F., & Plez, B. 1998, *A&A*, 333, 231
- Bogdanov, S., van den Berg, M., Heinke, C. O., et al. 2010, *ApJ*, 709, 241
- Bond, H. E., White, R. L., Becker, R. H., & O'Brien, M. S. 2002, *PASP*, 114, 1359
- Butters, O. W., Norton, A. J., Hakala, P., Mukai, K., & Barlow, E. J. 2008, *A&A*, 487, 271
- Cadelano, M., Pallanca, C., Ferraro, F. R., et al. 2015, *ApJ*, 807, 91
- Cohn, H. N., Lugger, P. M., Couch, S. M., et al. 2010, *ApJ*, 722, 20
- Cool, A. M., Grindlay, J. E., Cohn, H. N., Lugger, P. M., & Slavin, S. D. 1995, *ApJ*, 439, 695
- Cool, A. M., Grindlay, J. E., Cohn, H. N., Lugger, P. M., & Bailyn, C. D. 1998, *ApJ*, 508, L75
- De Marchi, G., Panagia, N., & Romaniello, M. 2010, *ApJ*, 715, 1
- Davies, M. 2005, *Advances in astronomy: From the Big Bang to the Solar System*, 1, 245
- Dotter, A., Chaboyer, B., Jevremović, D., et al. 2008, *ApJS*, 178, 89-101
- Edmonds, P. D., Grindlay, J. E., Cool, A., et al. 1999, *ApJ*, 516, 250
- Ferraro, F. R., Possenti, A., D'Amico, N., & Sabbi, E. 2001, *ApJ*, 561, L93
- Ferraro, F. R., Possenti, A., Sabbi, E., et al. 2003, *ApJ*, 595, 179
- Ferraro, F. R., Beccari, G., Dalessandro, E., et al. 2009, *Nature*, 462, 1028
- Ferraro, F. R., et al., 2012, *Nature*, 492, 393
- Ferraro, F. R., Lanzoni, B., Dalessandro, E., Mucciarelli, A., & Lovisi, L. 2015a, *Ecology of Blue Straggler Stars*, 99
- Ferraro, F. R., Pallanca, C., Lanzoni, B., et al. 2015b, *ApJ*, 807, L1
- Gratton, R. G., Bragaglia, A., Carretta, E., et al. 2003, *A&A*, 408, 529
- Grindlay, J. E., Cool, A. M., Callanan, P. J., et al. 1995, *ApJ*, 455, L47
- Grindlay, J. E. 1999, *Annapolis Workshop on Magnetic Cataclysmic Variables*, 157, 377
- Grindlay, J. E., Heinke, C. O., Edmonds, P. D., Murray, S. S., & Cool, A. M. 2001, *ApJ*, 563, L53
- Harris, W. E. 1996, *VizieR Online Data Catalog*, 7195,
- Holtzman, J. A., Burrows, C. J., Casertano, S., et al. 1995, *PASP*, 107, 1065
- Husser, T.-O., Kamann, S., Dreizler, S., et al. 2016, *A&A*, 588, A148
- Ivanova, N., Heinke, C. O., Rasio, F. A., et al. 2006, *MNRAS*, 372, 1043
- Kaluzny, J., Rucinski, S. M., & Thompson, I. B., 2003, *AJ*, 125, 1546
- Kaluzny, J., Thompson, I. B., Krzeminski, W., & Schwarzenberg-Czerny, A. 2006, *MNRAS*, 365, 548
- Knigge, C. 2012, *Mem. Soc. Astron. Italiana*, 83, 549
- Lanzoni, B., Ferraro, F. R., Alessandrini, E., et al. 2016, *ApJ*, 833, L29
- Lyne, A. G., Brinklow, A., Middleditch, J., Kulkarni, S. R., & Backer, D. C. 1987, *Nature*, 328, 399
- Pallanca, C., Dalessandro, E., Ferraro, F. R., et al. 2010, *ApJ*, 725, 1165
- Pallanca, C., Dalessandro, E., Ferraro, F. R., Lanzoni, B., & Beccari, G. 2013, *ApJ*, 773, 122
- Pallanca, C., Ransom, S. M., Ferraro, F. R., et al. 2014, *ApJ*, 795, 29
- Richer, H. B., Dotter, A., Hurley, J., et al. 2008, *AJ*, 135, 2141
- Roy, J., Ray, P. S., Bhattacharyya, B., et al. 2015, *ApJ*, 800, L12
- Sabbi, E., Gratton, R., Ferraro, F. R., et al. 2003, *ApJ*, 589, L41
- Shara, M. M., Hinkley, S., Zurek, D. R., Knigge, C., & Dieball, A. 2005, *AJ*, 130, 1829
- Stappers, B. W., Archibald, A. M., Hessels, J. W. T., et al. 2014, *ApJ*, 790, 39
- Stetson, P. B. 1987, *PASP*, 99, 191
- Stetson, P. B. 1994, *PASP*, 106, 250
- Taylor, J. M., Grindlay, J. E., Edmonds, P. D., & Cool, A. M. 2001, *ApJ*, 553, L169
- Townsley, D. M., & Bildsten, L. 2005, *ApJ*, 628, 395

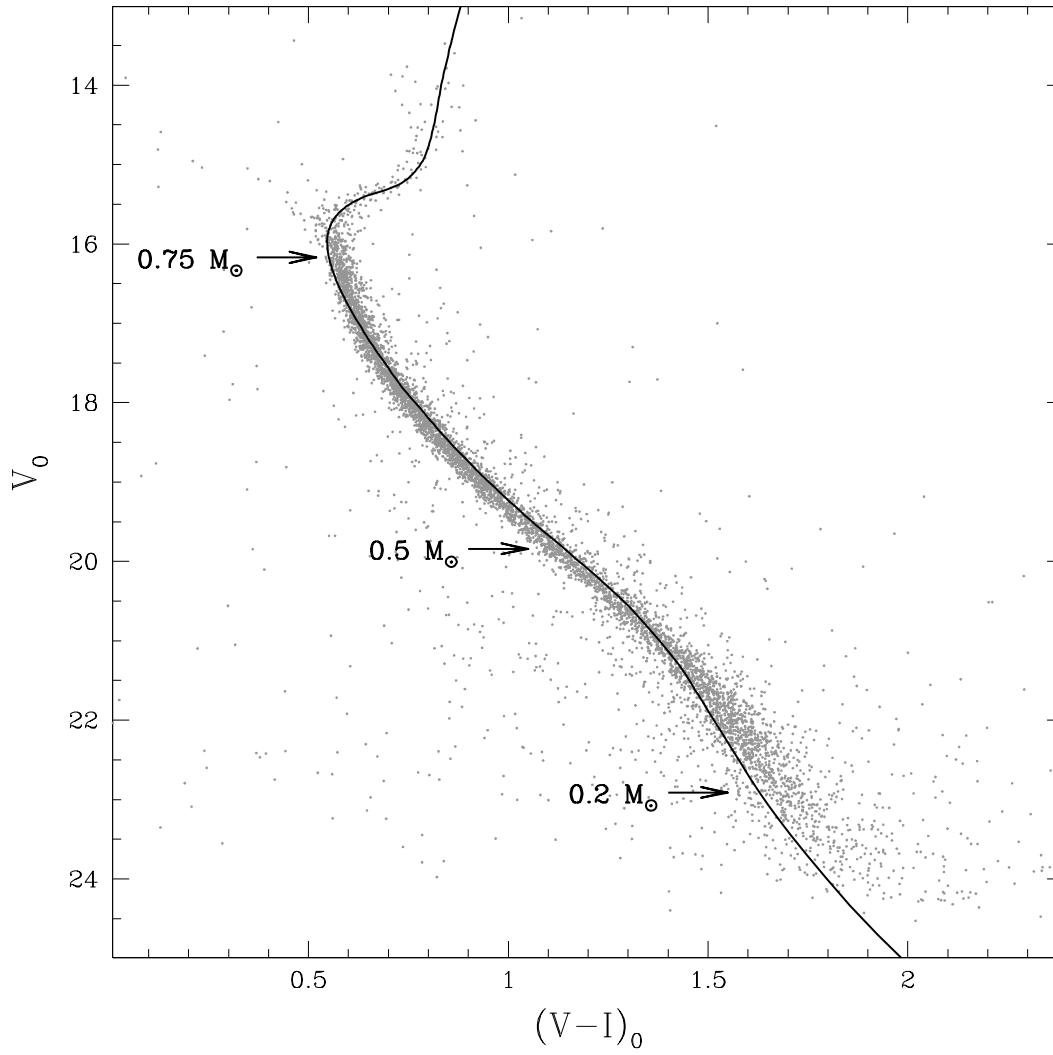


FIG. 1.— Reddening-corrected, optical color-magnitude diagram of NGC 6397. The black line indicates the location of the best-fit isochrone (age=13.5 Gyr, $[Fe/H] = -2.03$, $[\alpha/Fe] = 0.4$; Richer et al. 2008) assuming a reddening of $E(B-V) = 0.18$ and a distance modulus $(m-M)_0 = 12.01$. The location of stars with 0.2, 0.5 and $0.75M_{\odot}$ masses are labelled and marked with the arrows.

ID	RA J2000	Dec J2000	V ₀	I ₀	H α ₀	pEW Å	sEW Å	B10	G01	K06	T01	H16
CV1	265.1733338	-53.6720091	17.91	17.07	16.51	24.3±0.4	14.0±1.7-5.0±0.5 27.1±1.3-5.4±0.4 21 ^E ±0.9	U23	CV1	V12		10639
CV2	265.1762738	-53.6746139	19.14	18.07	17.64	21.0±0.4	30.2 ^E ±1.3	U19	CV2	V34		
CV3	265.1777106	-53.6720105	17.83	17.46	16.73	29.1±0.3	71.7 ^E ±2.8	U17	CV3	V33		
CV4	265.1742981	-53.6725857	19.70	18.65	17.26	90.4±1.0	106.7 ^E ±1.7	U21	CV4			
CV5	265.1737722	-53.6747031	20.68	19.62	18.26	87.4±1.4		U22	CV5			
CV6	265.2040901	-53.6634800	19.27	18.33	18.01	15.2±0.4	14.2±3.3-23.3±3.3	U10	CV6	V13		8919
CV7	265.1907295	-53.6782007	23.78	22.94	22.23	32.5±5.5		U11	CV7			
MSP-A	265.1859047	-53.6782108	16.43	15.68	15.66	3.2±0.2	3.0±0.1 3.8±0.2	U12		V16	BY (WF4-1)	4991
MSP?	265.1775326	-53.6743174	16.05	15.12	15.11	4.2±0.2	3.9±0.2 5.1±0.1	U18		V31	BY (PC-8) ?	5596
AB1	265.1788187	-53.6760517	17.26	16.41	16.46	1.9±0.2	2.9±0.2 2.9±0.2	U15			BY (PC-2)	5489
AB2	265.1689240	-53.6730075	17.79	16.90	16.95	2.3±0.2	2.9±0.3 3.0±0.7	U43			BY (PC-4)	10919
AB3	265.1669239	-53.6712405	19.63	18.40	18.49	3.2±0.4	2.2±0.8	U67				11027
AB4	265.1702716	-53.6714234	17.83	17.04	17.04	3.0±0.2	2.4±0.2 2.7±0.3	U69			BY (PC-5)	10841
AB5*	265.1779063	-53.6579716	18.36	17.50	17.57	1.5±0.2	2.0±0.4	U73				14084
AB6	265.1818423	-53.6751222	20.14	18.83	18.95	2.9±0.5		U75				
AB7*	265.1936621	-53.6875928	18.98	17.91	18.01	2.0±0.3	2.5±0.7 3.5±0.5	U81		V14		4580
AB8*	265.2022836	-53.6609875	19.02	17.98	18.09	1.5±0.2	1.9±0.8 2.0±0.7	U82			BY (WF2-1)	8990
AB9*	265.1786817	-53.6739516	17.37	16.58	16.64	1.2±0.2	2.4±0.3 3.0±0.5	U87			BY (PC-3)	5499
AB10	265.1784915	-53.6731722	16.56	15.90	15.93	1.3±0.2	1.5±0.2 1.8±0.1	U88		V19	BY (PC-1)	10230
AB11	265.1741289	-53.6707139	18.52	17.57	17.63	2.3±0.2	2.8±1.0 3.7±0.5	U90			BY (PC-6)	10564
1	265.1826286	-53.6782726	17.80	17.07	17.05	3.0±0.2	N.M.					5213
2	265.1792970	-53.6770140	18.27	17.47	17.50	2.2±0.3	N.M.					5438
3	265.1669335	-53.6582910	18.30	17.47	17.51	2.3±0.3	N.M.					14481
4	265.1869772	-53.6735069	18.31	17.49	17.54	1.8±0.2	N.M.					9678
5	265.1721989	-53.6682152	18.93	17.99	18.06	2.0±0.3	N.M.					10681
6	265.1743181	-53.6746601	19.45	18.30	18.41	2.1±0.3	N.M.					5917
7	265.2040749	-53.6776261	19.46	18.71	18.70	2.9±0.3						
8	265.1684970	-53.6574071	19.56	18.49	18.50	4.6±0.5						
9	265.1835070	-53.6748396	20.33	18.89	19.03	3.4±0.4						
10	265.1982481	-53.6658034	20.37	19.04	19.14	3.7±0.4					BY (WF3-4)	
11	265.2118907	-53.6617568	20.75	19.51	19.58	3.8±0.5						
12	265.1803621	-53.6782471	20.81	19.42	19.53	3.9±0.5						
13	265.1763986	-53.6829417	20.96	19.78	19.68	8.9±0.9						
14	265.2131393	-53.6744206	21.09	19.83	19.86	5.2±0.8						
15	265.2074017	-53.6694465	21.23	19.79	19.91	3.9±0.6						
16	265.1715432	-53.6897092	21.36	19.94	19.97	6.6±0.9						
17	265.1748629	-53.6915474	21.37	20.31	20.27	5.9±0.8						
18	265.1691896	-53.6571696	21.38	19.90	19.85	10.0±1.0						
19	265.1848957	-53.6763541	21.39	19.92	20.05	4.1±0.7						
20	265.2063740	-53.6654454	21.39	20.06	20.08	6.1±0.7						
21	265.2089910	-53.6693385	21.45	20.00	20.02	7.1±0.7						
22	265.1824425	-53.6817866	21.48	19.89	19.99	6.1±0.9						
23	265.1929464	-53.6694839	21.69	20.16	20.19	7.7±1.1						
24	265.2055337	-53.6651658	21.69	20.20	20.26	6.5±0.9						
25	265.1990390	-53.6602075	21.91	20.32	20.41	6.1±1.1						
26 ?	265.2121746	-53.6743002	22.08	20.52	20.56	7.8±1.1						
27 ?	265.1810287	-53.6956426	22.37	21.09	20.88	13.9±1.8						
28 ?	265.1688267	-53.6575723	22.43	20.73	20.38	25.0±2.6						
29 ?	265.1888864	-53.6906782	22.57	20.71	20.74	11.5±1.6						
30 ?	265.1739928	-53.6769901	22.77	20.60	20.61	19.8±2.7						
31 ?	265.1918767	-53.6491195	22.79	21.12	20.88	19.6±2.4						
32 ?	265.1921196	-53.6776013	23.26	21.22	20.94	30.2±3.1						
33 ?	265.1872843	-53.6910091	23.58	21.69	21.42	24.7±3.6						

TABLE 1

List of selected objects with H α excess. From left to right: Source Name, absolute coordinates, de-reddened magnitudes, photometric EW, spectroscopic EW (more than one value is reported if the line profile has been fitted by two gaussians, a second raw is added when more than one spectrum is available, the values marked by an "E" are the measures from Edmonds et al. 1999, N.M. means that although the spectra are available, has been impossible to measure the EW), list of IDs in papers available in the literature: B10=Bogdanov et al. 2010, G01=Grindlay et al. 2001, K06=Kaluzny et al. 2006 T01=Taylor et al. 2001 H16

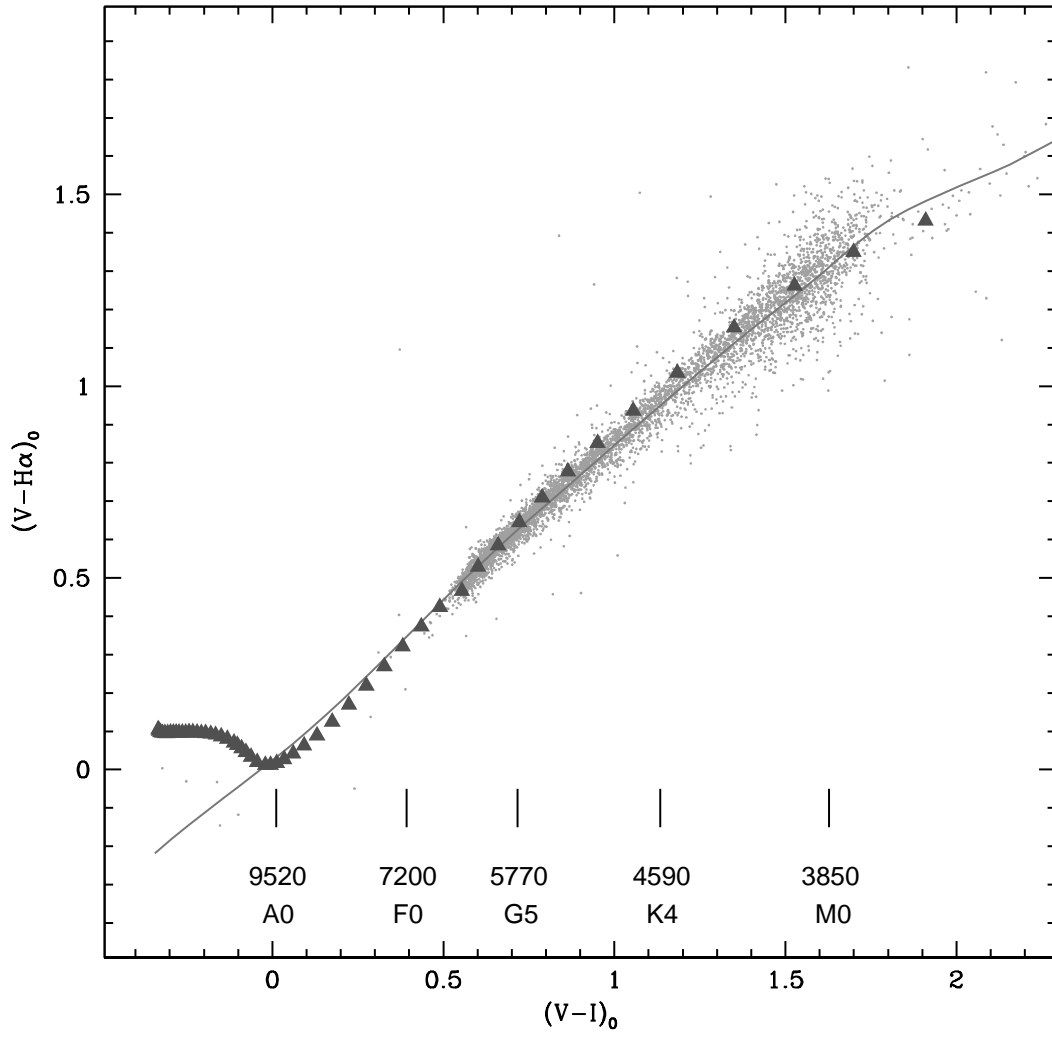


FIG. 2.— Reddening-corrected color-color diagram. The solid line is the median color of stars with no $H\alpha$ excess (gray dots) and hence the location of stars with $EWH\alpha = 0$. It corresponds well to the location (gray triangles) predicted by atmospheric models (Bessell et al. 1998). On the bottom part of the plot the MS spectral types and effective temperatures (in Kelvin) are reported for reference.

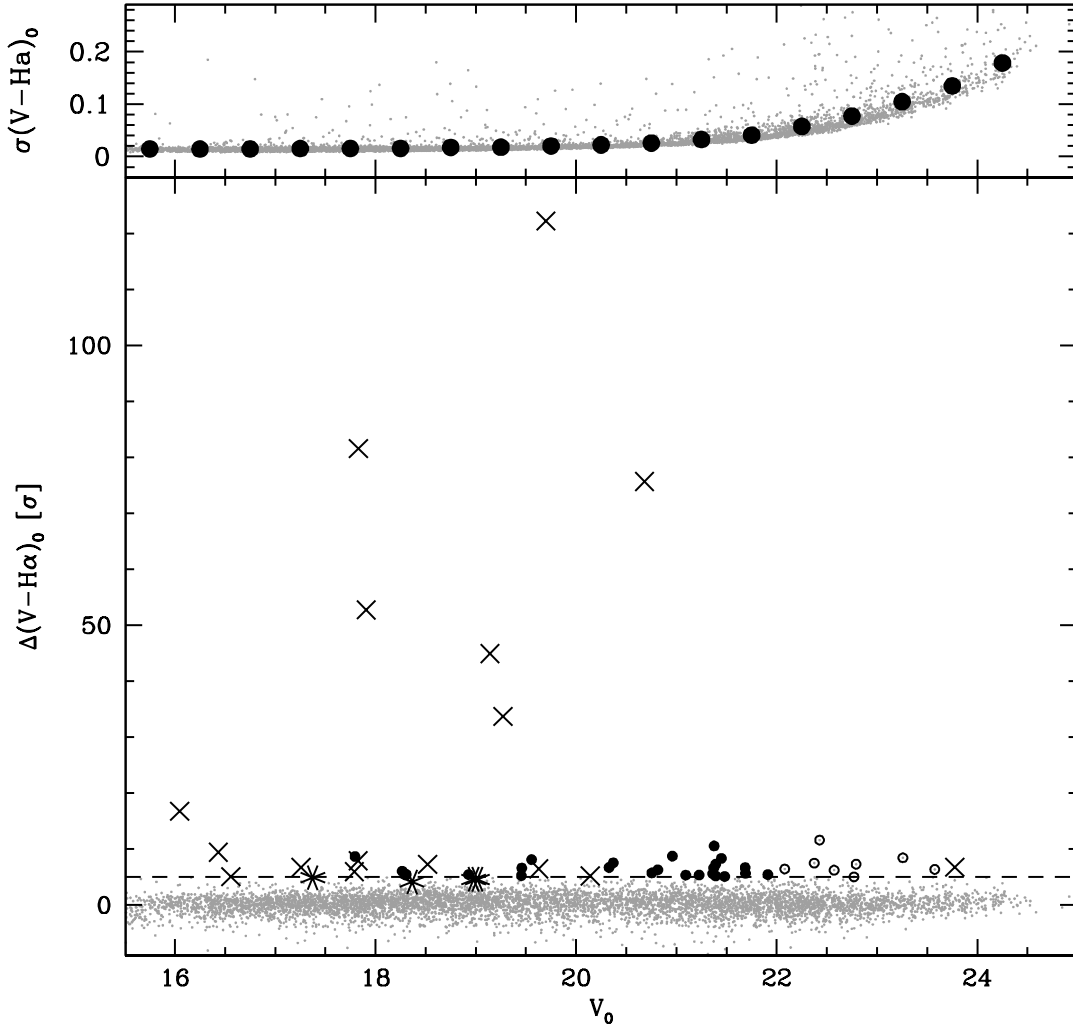


FIG. 3.— *Upper panel:* distribution of photometric errors as function of the magnitude V_0 . The large filled circles represent the average value of the photometric error of each 0.5 magnitude-wide bin. *Lower panel:* Color excess measured for each single star in unit of σ (upper panel). The dashed line corresponds to the 5 sigma threshold above which we selected the H α candidate emitters. The black crosses and dots correspond to the objects with and without the X-ray counterpart, respectively. The faintest objects ($V_0 > 22$), for which the classification is uncertain because of the large photometric errors, are plotted as open circles. The four objects marked by an asterisk correspond to X-ray counterparts selected (see Section 4.1 for more details).

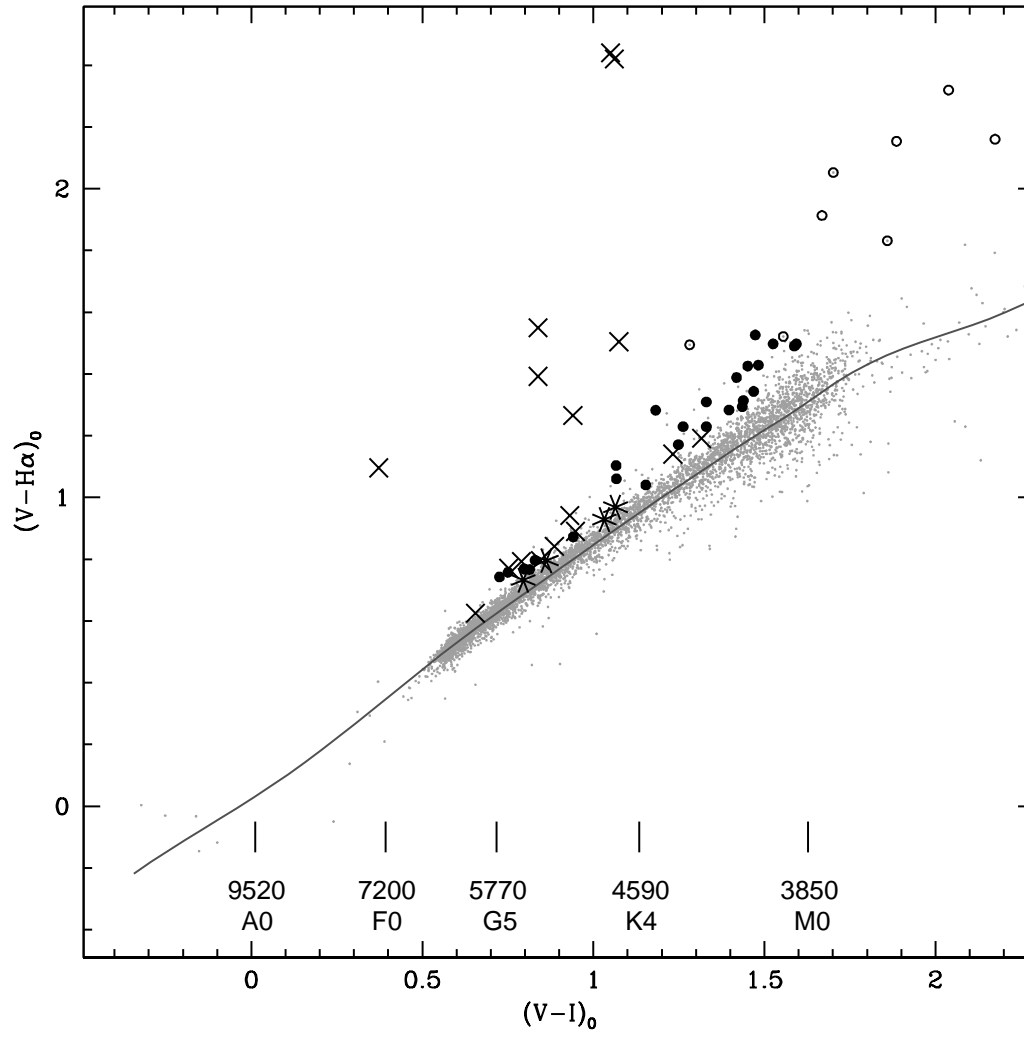


FIG. 4.— Same as Figure 2. We report here the location of objects with $H\alpha$ excess. The black crosses (or asterisks, see Figure 3) and dots correspond to the objects with and without the X-ray counterpart, respectively. The faintest objects ($V_0 > 22$), for which the classification is uncertain because of the large photometric errors, are plotted as open circles.

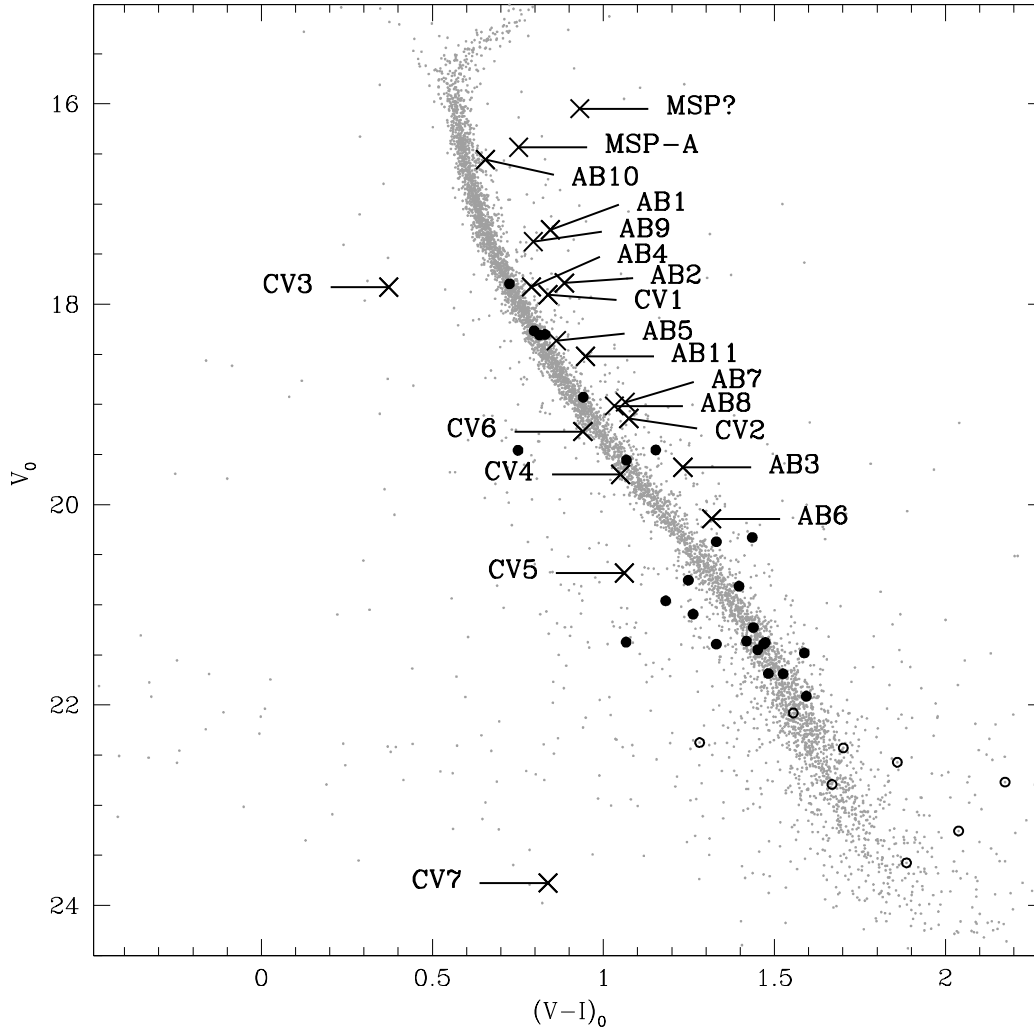


FIG. 5.— CMD location of object with H α excess. The black crosses and dots correspond to the objects with and without the X-ray counterpart, respectively. As in previous Figures, the faintest objects ($V_0 > 22$), for which the classification is uncertain because of the large photometric errors, are plotted as open circles. The names of sources with X-ray counterpart are reported for clarity.

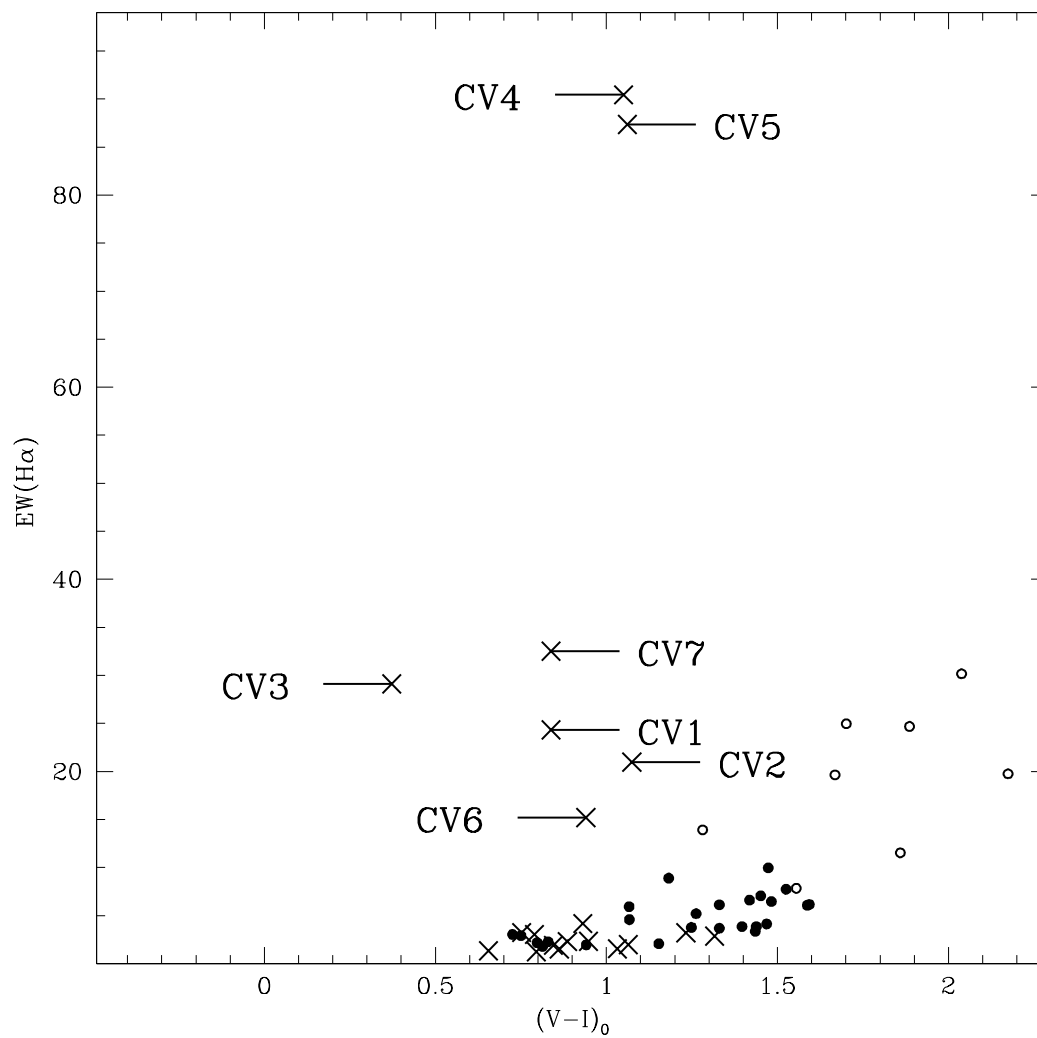


FIG. 6.— Estimated photometric EW of the emission, as a function of the color index representative of the spectral type. The symbols are as in the previous Figure. Names of known CVs are reported for clarity.

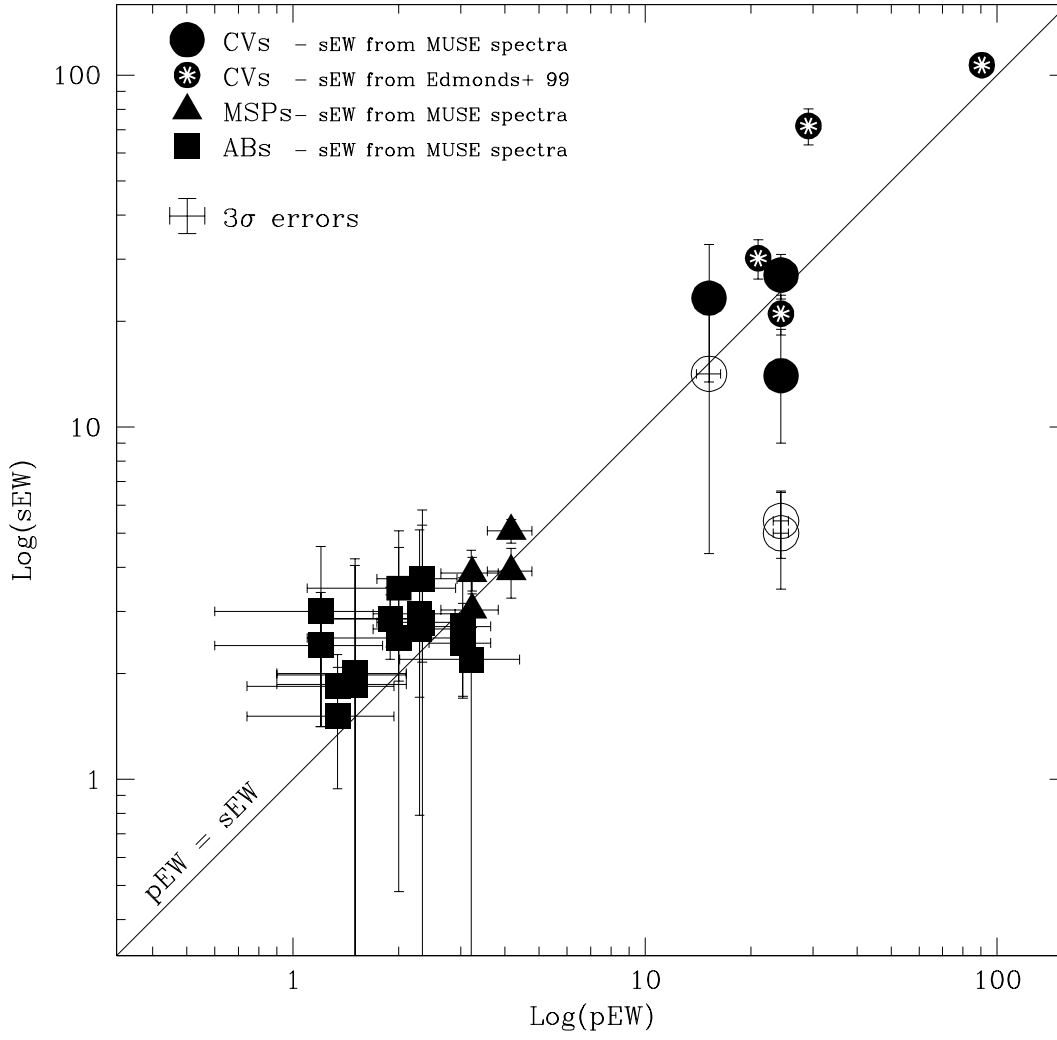


FIG. 7.— Spectroscopic EW measured from MUSE spectra as a function of the EWs estimated from photometry. For most of the targets more than one spectroscopic measure is shown. Different symbols correspond to different classes of objects as reported in the legend. The line corresponds to the locus of equality $\text{pEW} = \text{sEW}$. A clear correlation between the two independent EW measures is present in particular in the AB/MSP region. In the part of the plot where CVs are located the scatter is larger likely because of variations of the EW along the time. Note that in the Figure we plotted 3σ error bars, while the uncertainties reported in Table 1 are 1σ errors.

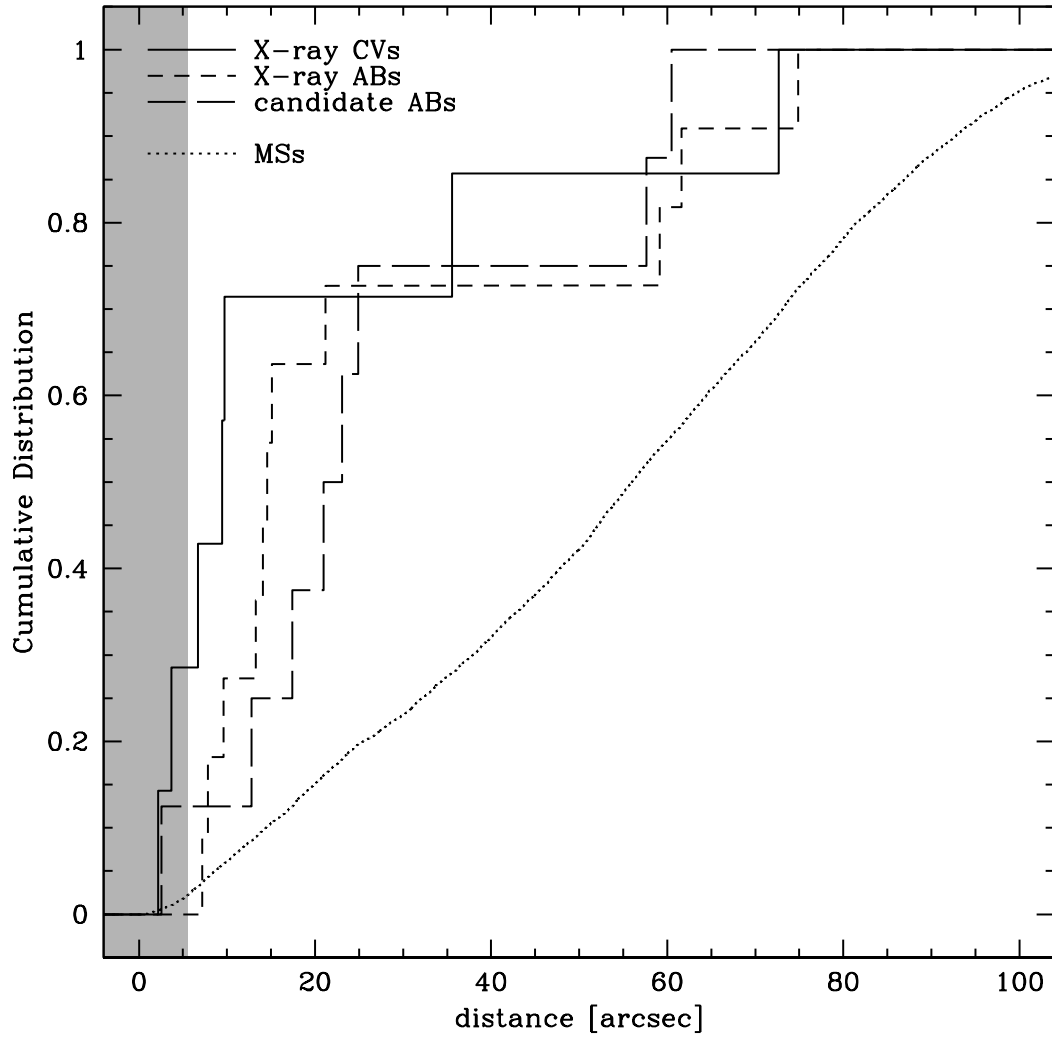


FIG. 8.— Cumulative radial distribution of different populations. In the top-left part of the plot the legend of different populations is reported. The shaded gray area represents the core radius ($5.5''$; Cohn et al. 2010). As evident the X-ray CVs and ABs as well as the candidate ABs are significantly more concentrated than MSs.